Int. J. Electrochem. Sci., 10 **(2015)** 5842 - 5861

International Journal of
ELECTROCHEMICAL
SCIENCE
www.electrochemsci.org

Parametric Simulations of Optimum Flow-field Configuration for Efficient Proton Exchange Membrane Fuel Cell

Vinh Nguyen Duy, Kyungcheol Kim, Jungkoo Lee, Jiwoong Ahn, Seongho Park, Taeeun Kim, Hyung-Man Kim[*]

Department of Mechanical Engineering & High Safety Vehicle Core Technology Research Center,
INJE University, 607 Eobang-dong, Gimhae-si, Gyongsangnam-do 621-749, Republic of Korea
[*]E-mail: mechkhm@inje.ac.kr

Received: 5 February 2015 / *Accepted:* 10 May 2015 / *Published:* 27 May 2015

The flow-field design of the uniform distribution of reacting gas generates broad scientific interest, especially among those who study the performances of proton exchange membrane fuel cell (PEMFC) in relation to pressure drop, discharge of condensed water, maximization of cell voltage, and uniformity of current density over the entire surface area. In this study, we characterize numerically two serpentine flow-fields of a new serpentine flow field with sub-channel and by-pass (SFFSB) driven by under-rib convection, and a conventional advanced serpentine flow field (CASFF). Under-rib convection enables a more effective utilization of the electrocatalysts by increasing the mass transport rates of the reactants from the flow channel to the inner catalyst layer and by significantly reducing the water flooding at the cathode. Four combinations of CASFF and SFFSB applied on the anode and cathode bipolar plates were compared each through a detailed numerical study of the distribution of temperature, pressure, water content, and local current density. In two flow-field configurations that SFFSB is applied at the cathode, the pressure drop is decreased because of the greater cross-sectional area for gas flow, and the decreased pressure drop results in the reduction of the load of BOP and accumulation of liquid water at the outlet. The anode liquid water mass fraction increases with increasing channel height because of increased back diffusion, while the cathode liquid water mass fraction does not depend upon the sub-channels which are ascribed mainly to the electro-osmotic drag. The current and power densities in the flow-field configuration that CASFF and SFFSB is applied at the anode and the cathode respectively are slightly higher than those in the flow-field configuration that SFFSB is applied at both the anode and the cathode. The findings in this work may make it possible to optimize the design of under-rib convection driven flow-field for efficient PEMFC.

Keywords: Polymer electrolyte fuel cell, Serpentine flow-field, Under-rib convection, Flow-field configuration, Polarization performance.

1. INTRODUCTION

The proton exchange membrane fuel cell (PEMFC) offer the possibility of cleaner electricity with less impact on the environment than the traditional energy conversion technologies, such as the automotive propulsion and the smart grid system [1]. One of the main obstacles to the commercialization of PEMFCs is the flow fields in the bipolar plate (BP) that cause severe water flooding and mass transport loss of the cathode. Nonetheless, the BP design as a whole and the flow channel layout configuration in particular have the potential to make an alternative clean power source compatible with its counterparts [2].

The presence of a convective flow in the under-rib regions enables an effective utilization of the electrocatalysts. This under-rib convection has recently been recognized as a non-negligible transport process that influences the performance of PEMFCs with serpentine flow fields [3-14]. Under-rib convection should not be ignored when the GDL permeability exceeds 10-13 m^2, which is consistent with the numerical prediction of the relative influence of under-rib convection [4, 5]. Experimental studies have shown that higher gas diffusion layer (GDL) permeability improves the performance of PEMFCs with serpentine flow fields [6-13]. Recently, the convection-enhanced serpentine flow field has been confirmed to have a better water handling ability than the conventional design [14], and the cathode flow field design for a single serpentine PEMFC has promoted strong convection flows to enhance oxygen transport and water removal [15].

The effects of various flow channel designs have been investigated by comparing the distribution of polarization, current density, and membrane water content at different cell voltages when changing the inlet humility operating conditions applied on four serpentine flow-field configurations: single channel, double channel, cyclic-single channel, and symmetric-single channel [16]. In the previous study, we also proposed a systematic design process for the serpentine flow field to enhance the performance of PEMFC through a detailed parametric study on each of the three different channel heights and widths [17-18]. A new serpentine flow field with sub-channels and by-passes (SFFSB) incorporated the experiments and the simulations to provide a better understanding and utilization of under-rib convective flow. The maximum current and power densities of the SFFSB were increased dramatically due to the promotion of under-rib convection than a conventional advanced serpentine flow field (CASFF). It has been understood that the flow field design plays a deterministic role in mass transport and water management, and thus great efforts have been made for optimal design of the flow field that would guarantee high and stable cell performance.

In this study, four combinations of CASFF and SFFSB applied on the anode and cathode bipolar plates are numerically analyzed to study the performances of PEMFC in relation to pressure drop, discharge of condensed water, maximization of cell voltage and uniformity of current density over the entire surface area. The comparative analysis was conducted on four configurations as listed: a configuration Ⅰ in which both CASFFs used at the anode and the cathode, a configuration Ⅱ in which CASFF and SFFSB used at the anode and the cathode respectively, a configuration Ⅲ in which SFFSB and CASFF used at the anode and the cathode respectively, a configuration Ⅳ in which both SFFSBs used at the anode and the cathode. We propose a systematic design process for the serpentine flow-field configuration to enhance the performance of PEMFC through a detailed parametric study on each of the four combinations of CASFF and SFFSB applied on the anode and cathode bipolar plates.

2. NUMERICAL MODEL

Table 1. Parameters and symbols used in this modeling.

Nomenclature	
α_k	Activity of water in stream *k*, dimensionless
C_{wk}	Concentration of water vapor at *k*th interface of the membrane, mol/m^3
D_w	Diffusion coefficient of water, m^2/s
F	Faraday constant 96487 C/mole-of-electrons
I	Local current density, A/m^2
$M_{m,dry}$	Equivalent weight of a dry membrane, kg/mol
η_d	Electro-osmotic drag coefficient
$P_{w,k}^{sat}$	Vapor pressure of water in stream k, Pa
P	Pressure, Pa
t_m	Membrane thickness, m
V_{OCV}	Cell open-circuit voltage, V
V_{cell}	Cell voltage, V
$X_{w,k}$	Mole fraction of water in stream *k*
α	Net water flux per proton flux
α_a	Anode transfer coefficient

η	Overpotential for oxygen reaction, V
λ	Water content in the membrane
$\rho_{m,dry}$	Density of a dry membrane, kg·m^{-3}
σ_m	Membrane conductivity, ohm^{-1}·m^{-1}
k	Anode or cathode
w	Water
sat	saturated

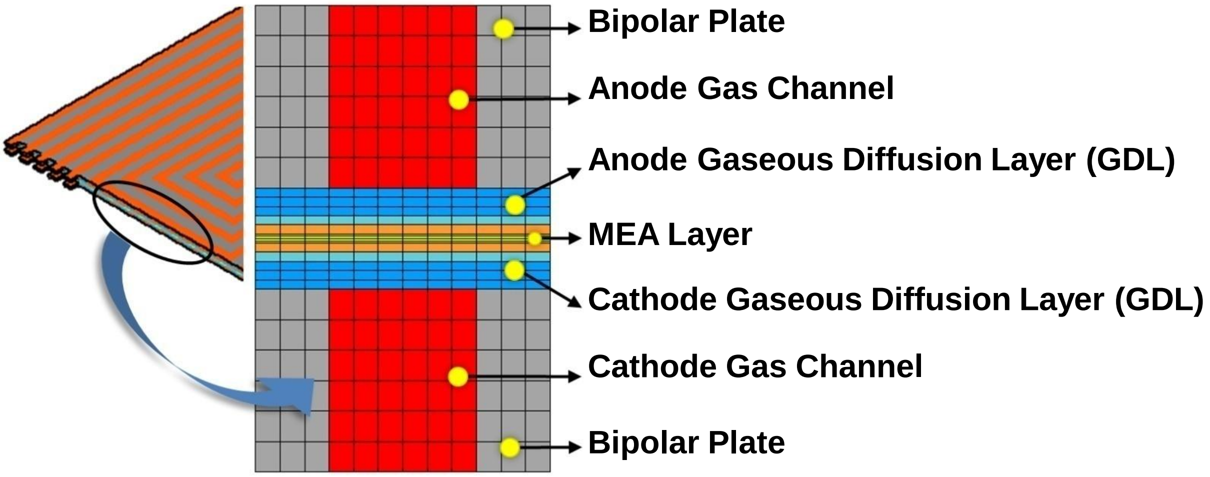

Figure 1. Schematic illustration of a computational domain for PEMFC simulation [17]

The model equations were solved using the commercial computational fluid dynamics (CFD) software ANSYS Fluent® 14.5, a commercial finite volume technique solver, which has the requirement of the source terms for species transport equations, heat sources and liquid water formation [19]. The parameters and symbols used in the modeling are summarized in Table 1. In the modeling of the PEMFC the following assumptions were made: the cell operates under steady-state condition, isothermal boundary conditions were used for external walls, flow in the cell is considered to be laminar, reactant and products are assumed to be ideal gas mixtures, and the electrode is assumed to be an isotropic and homogenous porous medium.

Fig. 1 shows a schematic diagram of a typical computational domain for PEMFC consisting of two bipolar plates, anode/cathode gas channels, anode/cathode gas diffusion layers (GDLs) and MEA on 25 cm^2 active area [17]. It was assumed that the fuel was hydrogen at the anode side, diffuses through the porous gas diffusion layers and come in contact with the catalyst layer. At this layer, it forms hydrogen ions and electrons. The hydrogen ions diffuse through the proton exchange membrane at the center while the electrons flow through the gas diffusion layer to the current collectors and into the electric load attached. The details of the flow-field and other physical parameters used for the base case are summarized in Table 2.

Table 2. Physical details of parameters and properties used in this modeling.

Physical parameters and properties	
Current conductivity	5.7 $W \cdot m^{-1} \cdot K^{-1}$
Electric conductivity	10,000 $\Omega^{-1} \cdot m^{-1}$
Thickness after compressed	250 μm
Permeability of GDL	1.0e-12 m^2
Tortuosity of GDL	1.5
Porosity after compressed	70 %
Diffusion adjustment	50 %
Thermal conductivity	0.21 $W \cdot m^{-1} \cdot K^{-1}$
Thickness of MEA (catalyst layer)	50 μm (12.5 μm)
Thermal conductivity	0.15 $W \cdot m^{-1} \cdot K^{-1}$
Dry membrane density	2.0 $g \cdot m^{-3}$
Equivalent weight of dry membrane	1,100 $g \cdot mol^{-1}$
Cathode exchange current density	0.02 $A \cdot cm^{-2}$
Cathode transfer coefficient	0.6
Anode exchange current density	0.2 $A \cdot cm^{-2}$
Anode transfer coefficient	1.2

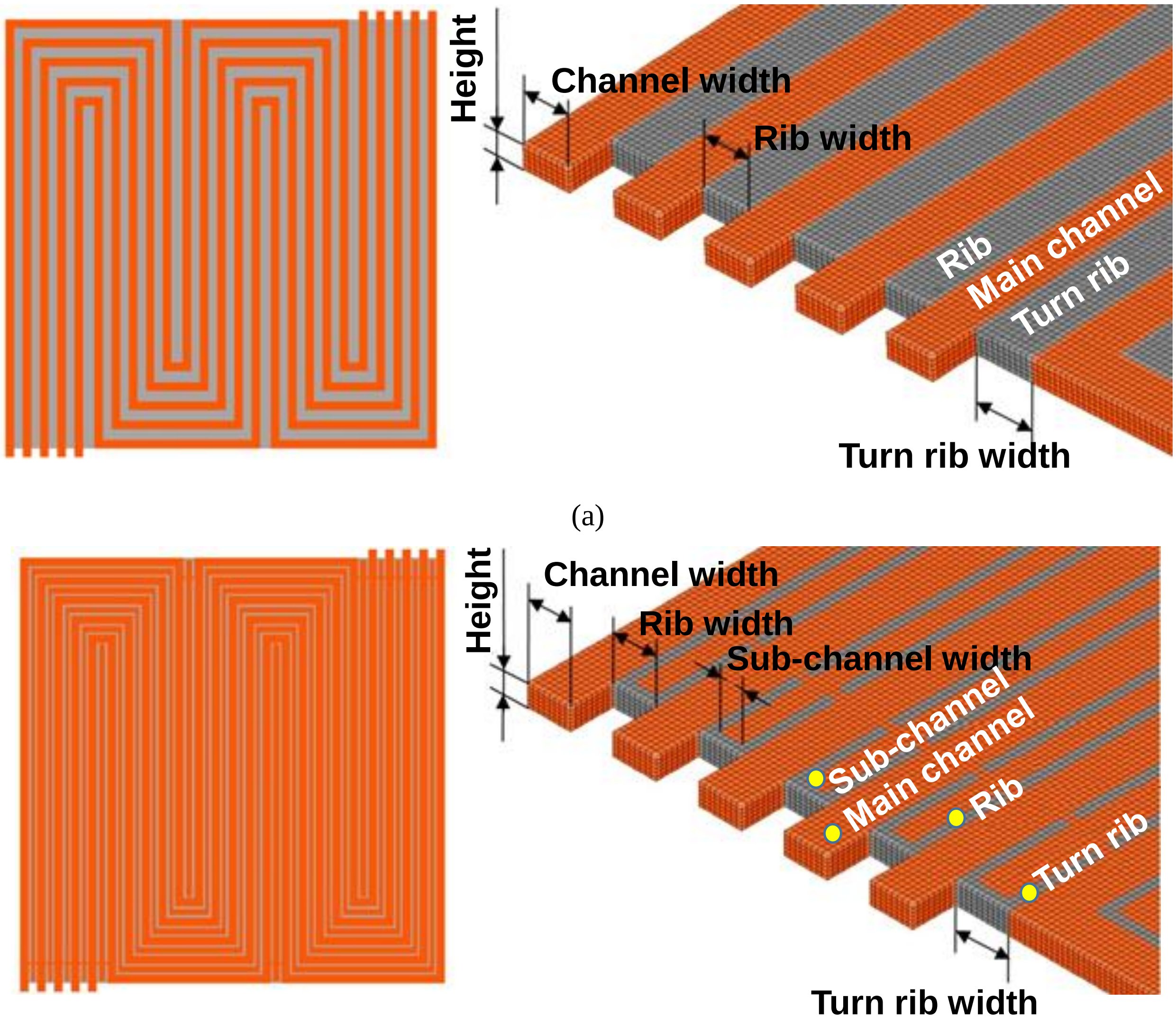

(a)

(b)

Figure 2. Two serpentine flow-field configurations of 5-passes and 4-turns on 25 cm^2 active area; (a) CASFF, (b) SFFSB

As shown in Fig. 2, two 25 cm^2 serpentine flow-fields of 5-passes and 4-turns were considered in this study. Through the previous geometrical characterization of serpentine flow channels with various heights and widths, a CASFF was selected as a design standard. As the presence of under-rib convection enables more effective utilization of electrocatalysts by increasing reactant concentration and facilitating liquid water removal. We designed two 25 cm^2 serpentine flow-field patterns of 5-passes and 4-turns; (a) CASFF, (b) SFFSB as shown in Fig. 2 to stimulate the under-rib convection. The geometric details of the above two flow-fields are listed in Table 3 [10].

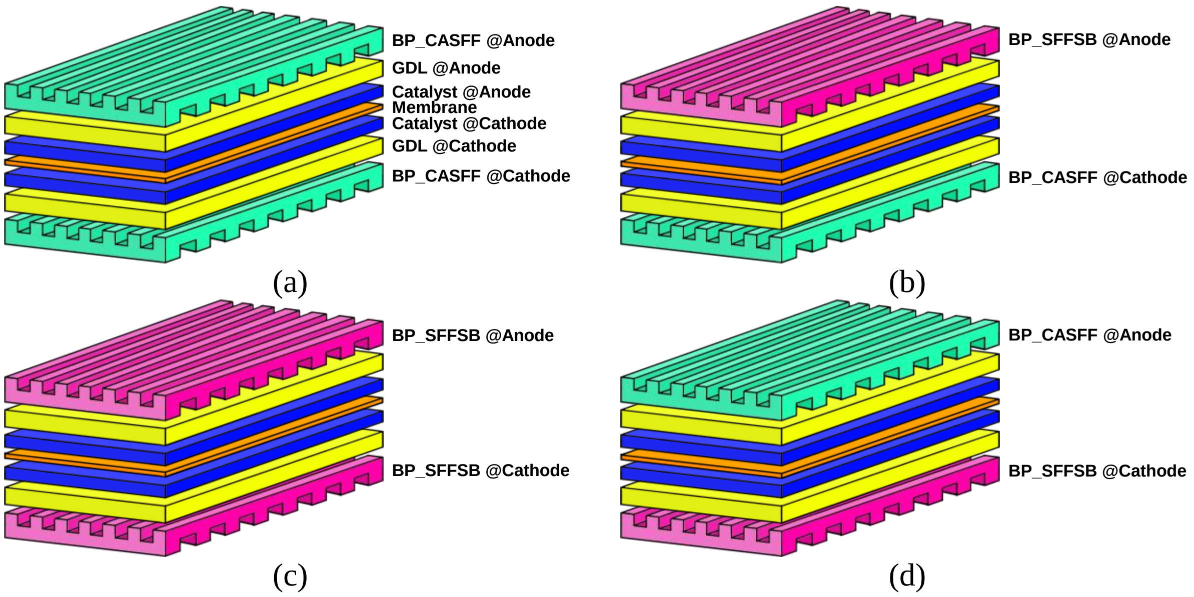

(a) (b)

(c) (d)

Figure 3. Four combinations of CASFF and SFFSB applied on the anode and cathode bipolar plates; (a) configuration Ⅰ: both CASFFs used at the anode and the cathode, (b) configuration Ⅱ: CASFF and SFFSB used at the anode and the cathode respectively, (c) configuration Ⅲ: SFFSB and CASFF used at the anode and the cathode respectively, (d) configuration Ⅳ: both SFFSBs used at the anode and the cathode.

As shown in Fig. 3, numerical simulations were performed to compare the four configurations; a configuration Ⅰ in which both CASFFs used at the anode and the cathode, a configuration Ⅱ in which CASFF and SFFSB used at the anode and the cathode respectively, a configuration Ⅲ in which SFFSB and CASFF used at the anode and the cathode respectively, a configuration Ⅳ in which both SFFSBs used at the anode and the cathode.

Table 3. Geometric details of two flow-field configurations used in this modeling.

Flow-field configuration	CASFF	SFFSB
Main channel width [mm]	1.0	1.0
Main channel rib width [mm]	1.0	1.0
Main channel turn rib width [mm]	1.25	1.25
Sub-channel width [mm]	-	0.5
Sub-channel turn rib width [mm]	-	0.75
Main channel height [mm]	0.5	0.5

Sub-channel height [mm]	-	0.334
Cross-sectional area [cm^2]	0.25	0.025

Numerical modeling is performed based on a single-domain formulation by calculating the source terms given in Table 1, with the assumption of a steady state, ideal gas properties, and homogeneous two phase flows for mass transport through channels and GDL. Therefore, the cell size of the mesh layer used in the channel and rib regions has little influence on numerical calculation. The pressure, temperature, water content, and current density distributions at the membrane/electrode interface were calculated numerically by cell (mesh), and we composed the cell (mesh) size of GDL and MEA densely. On the other hand, the cell size in the mesh layer used for the numerical calculation in the channel and rib regions was 0.16 mm in height and 0.25 mm in width, which were bigger than those of 0.125 (MEA) and 0.05 (GDL) mm in height and 0.05 mm in width in the GDL and MEA region.

To improve the computational accuracy, grid cells were established by equalizing the node connectivity in each component and by using the hexahedron mesh. Consequently, about a half million computational cells are involved in all geometries. For the solution procedure to solve the flow-field, the SIMPLE algorithm was applied with an algebraic multi-grid method. The present numerical model was validated by grid tests and numerical simulation results on 10 cm^2 serpentine with a single channel flow-field PEMFC [17]. The maximum aspect ratio and skewness of meshes are limited to 20 and 0.5, respectively. The convergence criterion for the mass balance and energy balance is 1 % with a maximum residual tolerance of 1E-07.

3. RESULTS and DISCUSSION

Table 4. Inlet and operating conditions used in this modeling.

Inlet conditions	
Mass flow rate inlet	6.01e-6 $kg\cdot s^{-1}$
Inlet temperature	75 ℃
Mass fraction of hydrogen	0.078
Mass fraction of water	0.561
Mass fraction of nitrogen	0.361
Mass flow rate inlet	3.03e-5 $kg\cdot s^{-1}$

Inlet temperature	75 ℃
Mass fraction of Oxygen	0.169
Mass fraction of water	0.274
Exit pressure	101 kPa
Open circuit voltage	0.96 V
Cell temperature	75 ℃

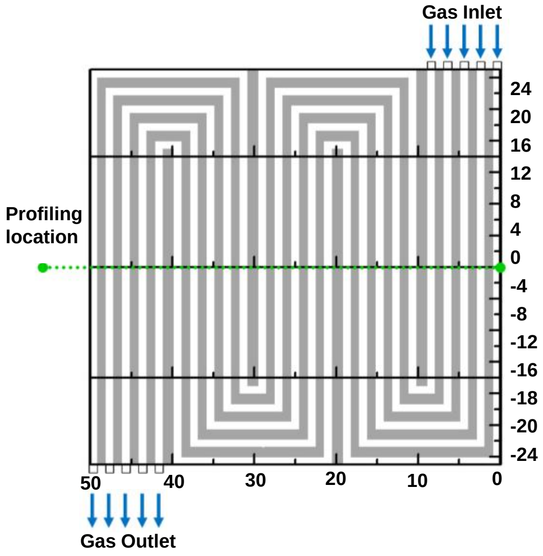

Figure 4. Index and location of the serpentine flow-field for profiling the performance-related parameters [17]

The membrane water content and the phenomena of mass transport and electrochemical reactions in the anode side and the cathode side are diverse and complex. Consequently, to enhance fuel cell performance, flow field in the BPs should be designed flexibly to adapt operating conditions. However, most of PEMFC devices normally use the same flow field BPs design for both anode and cathode. In this research, we propose a numerical analysis to compare fuel cell performances when flexibility using CASFF and SFFSB design for anode and cathode bipolar plate and evaluate the best design flow field for fuel cell application.

The parametric studies were conducted on 25 cm^2 serpentine bipolar plates of PEMFC that have the four flow-field configurations, all under the same operating conditions as listed in Table 4. The performance of PEMFC was analyzed by using the present numerical model of the electrochemical reaction and transport phenomena which are fully coupled with the governing equations. Therefore as shown in Fig. 4, the distributions of performance-related parameters are profiled and compared quantitatively at the same location [10]. The performance-related parameters include the total pressure, hydrogen and oxygen mass fraction, liquid water mass fraction, temperature, membrane water content and liquid water activity, and current density. They are investigated to generate the optimum flow-field configuration that enhances the performance of PEMFC. The optimization of the flow-field configuration is discussed in relation to the minimization of pressure drop, the smooth discharge of condensed water, the uniformity of current density over the entire surface area as well as the maximization of cell voltage at I_{avg} of 1.0 A/cm^2.

3.1 Comparison of the performance-related parameter distributions

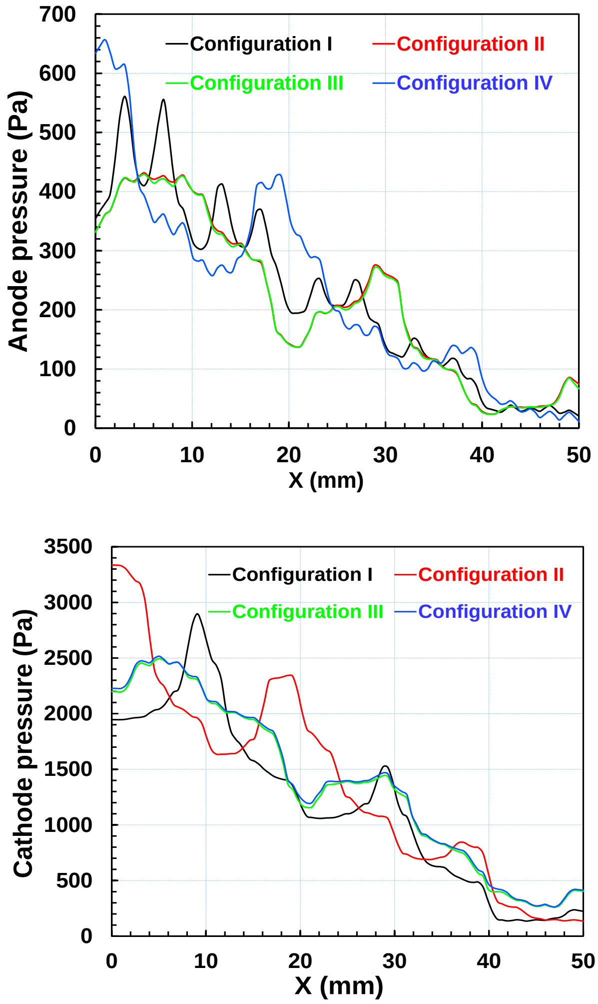

Figure 5. The comparison of the total pressures on the anode and the cathode side between the four flow-field configurations #I-Ⅳ at I_{avg}=1.0 A/cm^2.

The performance-related parameter distributions of the four flow-field configurations are compared at the averaged current density of 1.0 A/cm^2. The total pressures on the anode and the cathode decrease from the inlet toward the outlet as shown in Fig. 5 because of the pressure drop caused by the frictional and bending losses in the gas flow channel [17]. The pressure drop at the corresponding location between the adjacent channels would be substantial, and a significant pressure gradient is thus set up across the porous electrode, a pressure gradient much larger than that along the channel direction, which results in a considerable cross-leakage flow between the adjacent channels. In fact, this flow induces a strong convection in the electrode, bringing the reactants to the catalyst layer and removing the product water from the reaction sites and electrodes. This flow is responsible for the improvement in overall performance.

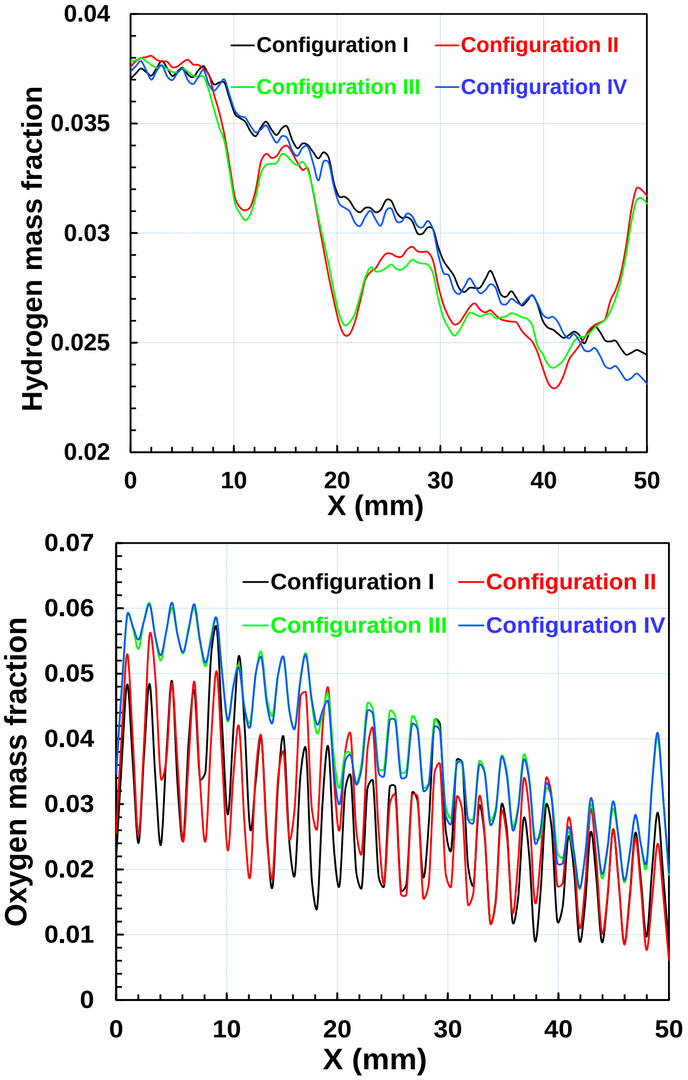

Figure 6. The comparison of the hydrogen and oxygen mass fractions between the four flow-field configurations #I-IV at I_{avg}=1.0 A/cm^2.

As shown in Fig. 6, hydrogen and oxygen mass fractions decrease almost equally from the inlet toward the outlet because the four flow-field configurations Ⅰ-Ⅳ have equal electrochemical reaction. However, the cross-leakage flow set up by the pressure difference between the adjacent channels enhances electrochemical reaction, and the reactant concentration between the electrode and the catalyst layer is influenced by the cross-leakage flow. As the channel height increases, the pressure difference is decreased; therefore, hydrogen and oxygen mass fractions are also decreased.

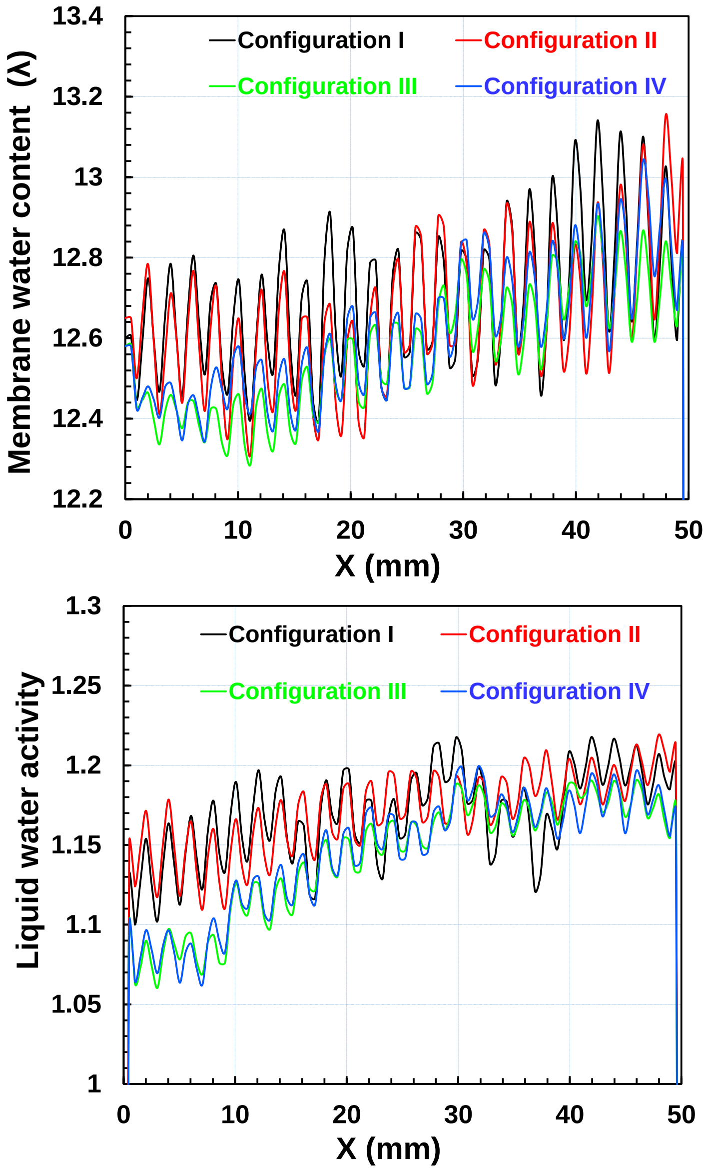

Figure 7. The comparison of the membrane water content and liquid water activity between the four flow-field configurations #I-IV at I_{avg}=1.0 A/cm^2.

The membrane water content depends on the water activity affected by the total pressure. Fig. 7 shows that the membrane water content under the rib areas is higher than that under the adjacent channel areas because much of the water produced between GDL and the rib is absorbed into the membrane by under-rib convection. The under-rib convection denotes the same process as the cross-leakage flow [17]. The membrane water content increases from the inlet toward the outlet due to the decrease of total pressure. The electro-osmotic drag coefficient as a function of the membrane water content affects the net water flux per proton which expresses the water transport between anode and cathode. If the net water flux per proton is greater than 0, the electro-osmotic drag is higher than the back diffusion, and water is transported from the anode to the cathode.

Fig. 7 shows that the liquid water activity fluctuates between the peak under the channels and the trough under the ribs, and the variation increases from the inlet toward the outlet. The net water flux per proton is less than 0 in the outlet area under the ribs, and water is transported from the cathode to the anode by the back diffusion. This phenomenon increases slightly as the channel height increases, as it was confirmed by the anode and cathode liquid water mass fractions. Liquid water mass fraction also fluctuates between the peak under the channels and the trough under the ribs, and the variation increases from the inlet toward the outlet. As the channel height increases, liquid water mass fraction on the anode side increases due to the back diffusion and the low pressure drop.

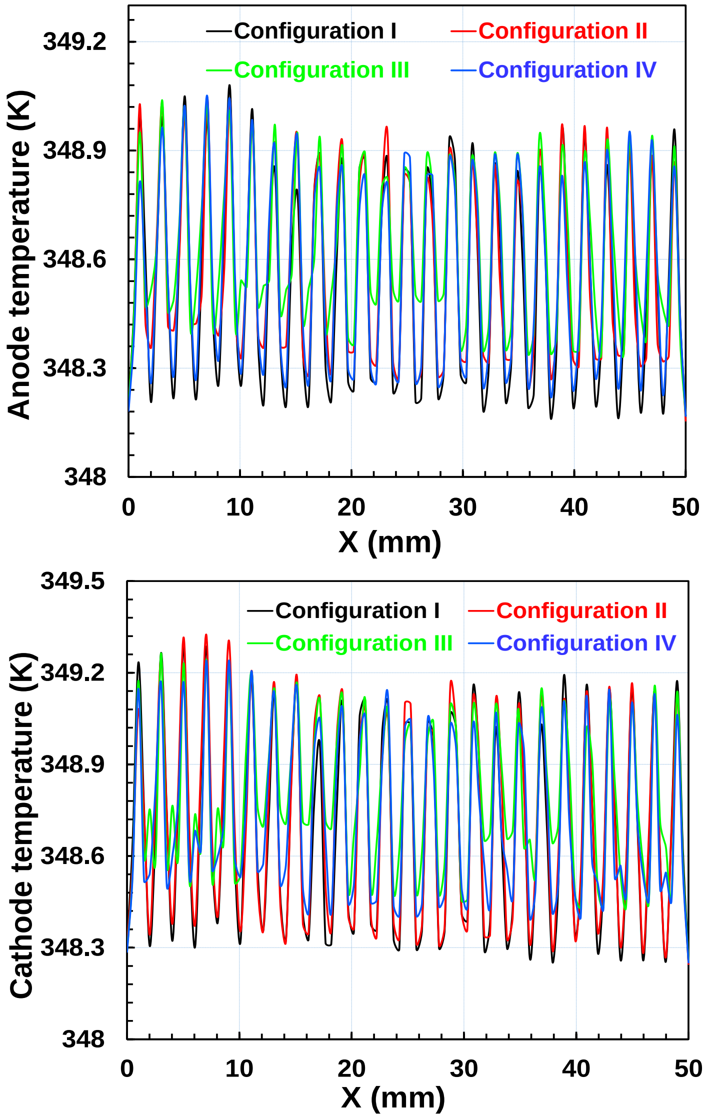

Figure 8. The comparison of the temperatures on the anode and the cathode side between the four flow-field #I-IV at I_{avg}=1.0 A/cm^2.

It has an influence on water remove inside PEMFC, and then anode liquid water mass fraction increases. On the other hand, the liquid water mass fraction on the cathode side remains almost the same mainly because of the electro-osmotic drag even with the channel height increase. The local temperatures on the anode and cathode side are shown in Fig. 8. Since the cathode membrane interface is the location where the most heat generation occurs, the temperature on the cathode side is higher than that on the anode side. The temperature under the rib areas was found to be lower than that under the adjacent channel areas because the heat produced in the area under the ribs is more easily transferred to the graphite block compared to the heat produced in the area under the channels. Temperature decreases from the inlet toward the outlet due to the cooling of the liquid water at the outlet. As the channel height increases, the temperature increases because of the smaller heat transfer that can remove heat with longer distance.

3.2 Comparison of the liquid water behaviors

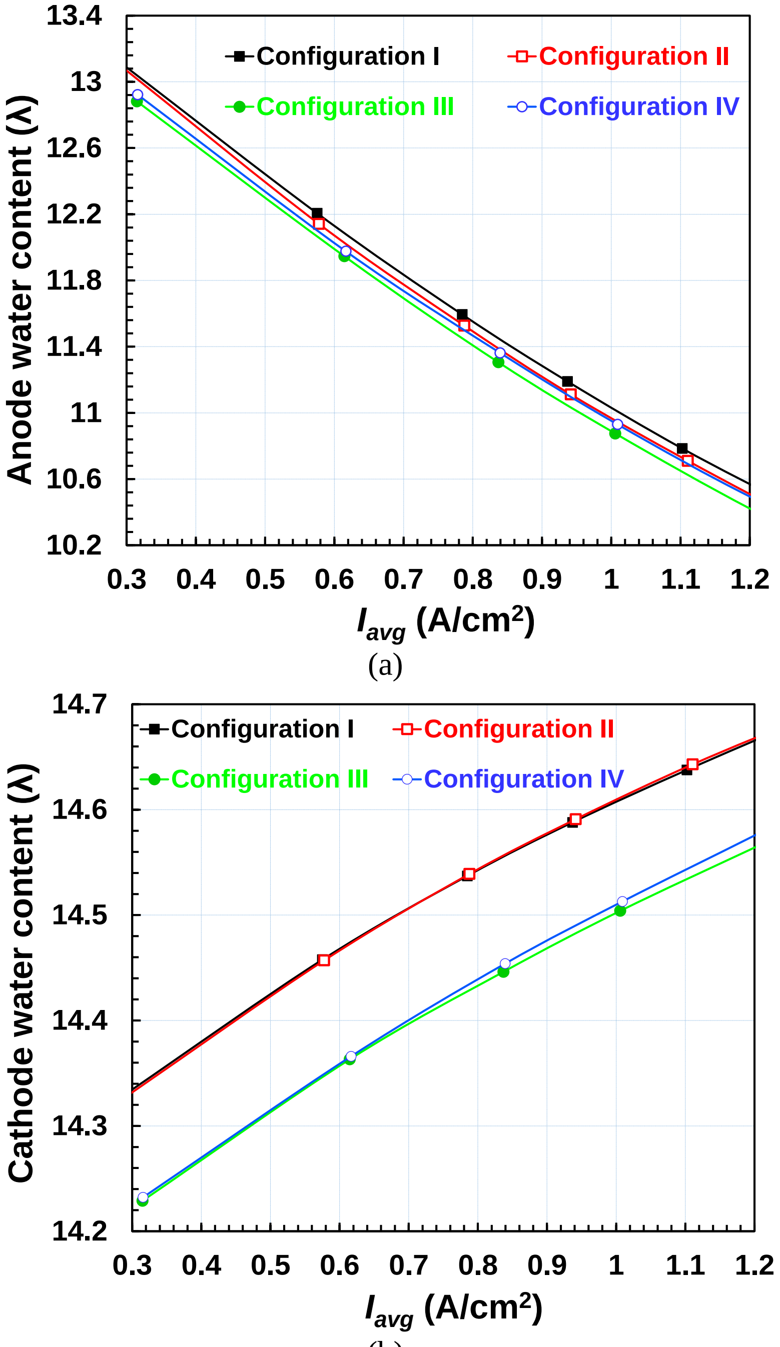

(a)

(b)

Figure 9. The comparison of the average water content on the (a) anode and (b) cathode catalysts between the four flow-field configurations #I-Ⅳ.

The average water content of the membrane, the anode and the cathode catalysts are compared between the four flow-field configurations Ⅰ-Ⅳ at various current densities, as shown in Fig. 9. The water content increases from the anode to the cathode and reaches maximum at the cathode catalyst because the contents of membranes and anode catalysts reduce when increasing current density [10]. However, there is an opposite trend in the cathode catalysts when their water contents increase with growing current density. These phenomena can be explained because an increasing current density results in an increase of the amount of water in the cathode catalyst because back diffusion is not high enough to compensate electro-osmotic drag in drying phenomena of the anode, and the anode drying shows faster progress than the velocity of moving water [13].

For a fully humidified condition a membrane water content value of λ=14 is appropriate. Therefore, it is assumed that the flooding phenomenon is occurred at a location in the range of λ over 14 [11]. All the simulation results show that the average water content of membrane is under 14, thus the water flooding is predicted not to be significant at the membranes. However, it may be still occurred in the cathode catalyst areas at where the water contents are very high, though the water contents in all anode catalysts are smaller than the value of λ=14 dramatically. These results can be seen clearly in an increment of the average water saturations (liquid saturation) in the cathode catalysts and the gas diffusion layers when increasing current densities in all simulated cases. The average liquid water in configurations Ⅰ and Ⅱ is higher than this of configurations Ⅲ and Ⅳ significantly. Consequently, the flooding phenomena of cathode flooding in configurations Ⅰ and Ⅱ is more seriously which results in hindering transport of the reactant species by blocking the pores in the porous gas diffusion layer and by covering up the active sites in the catalyst layer, as a result, the power density of configurations Ⅲ and Ⅳ is higher than configurations Ⅰ and Ⅱ at a same current density.

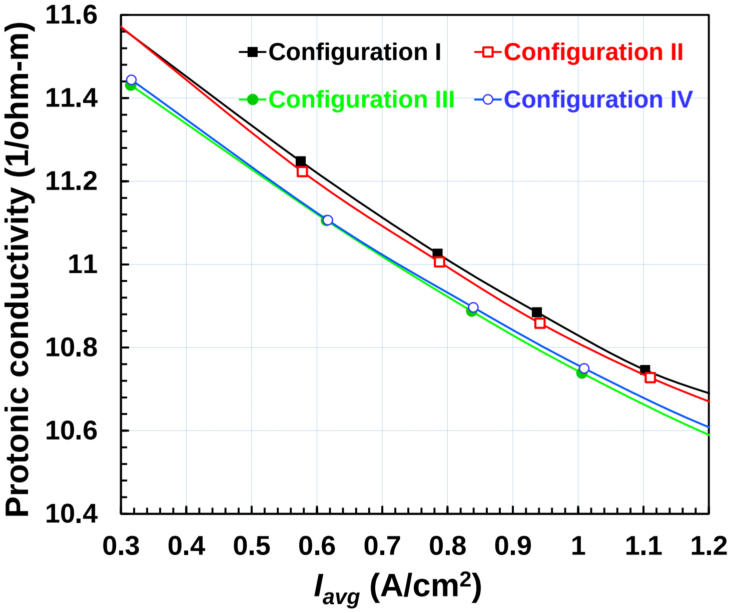

Figure 10. The comparison of the membrane protonic conductivity between the four flow-field configurations #I-IV.

The high membrane conductivity relates to the reduction of internal resistance and voltage drop; therefore, configuration Ⅲ has higher density just by 0.8 % than configuration Ⅳ. As shown in Fig. 10, the water content of the anode catalyst and the membrane of configuration Ⅲ are somewhat higher than that of configuration Ⅳ, and thus the average membrane conductivity of configuration Ⅲ is higher than that of configuration Ⅳ. On the other hand, in configurations Ⅰ and Ⅱ, the liquid water content in the cathode side is high; therefore, the anode drying increases the back diffusion from the cathode side to the anode side resulting for reducing the liquid water in the cathode catalyst and GDL.

Figs. 11 and 12 present the liquid water distributions at cathode channels and reference location determined at the current density of 1.0 A/cm^2. The liquid water content increases from the inlet toward the outlet and from the cathode side to the cathode side; furthermore liquid water appearing in anode sides is not appreciable in all simulated cases. However, in cathode side, the liquid water distribution of configurations Ⅰ and Ⅱ is higher than configurations Ⅲ and Ⅳ.

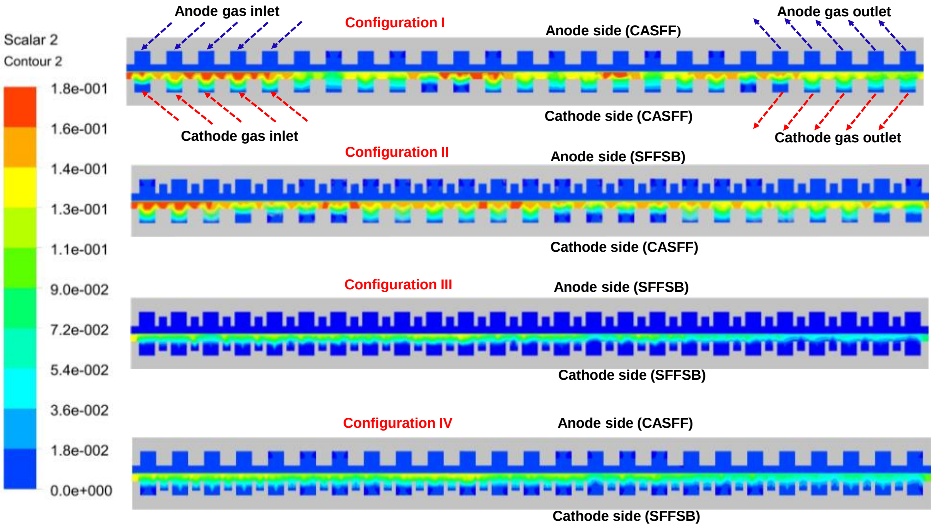

Figure 11. The comparison of the liquid water distibution at the reference location between the four flow-field configurations #I-IV at I_{avg}=1.0 A/cm^2.

These phenomena can be explained by the effect of changeable flow-field configuration on water accumulation of the PEM fuel cell. In case of CASFF for the bipolar plate, under-rib convection is generated from the inlet to the outlet direction due to high stoichiometry ratio, and high velocity vectors are observed adjacent rib and turn-rib area. Consequently, the reacting gases migrate to the adjacent main channel through the bottom of the rib from the inlet to the outlet direction. And in case of SFFSB, since a sub-channel is inserted in-between the main channels, flow direction of under-rib convection is changed from the main channel to the sub-channel based on the sub-channel due to the difference of pressure between the sub channels therefore improving gas permeability and overall gas diffusion force. Furthermore, water generated in the rib area is emitted to the sub-channel and discharged toward the outlet; as a result, the water flooding phenomena can be reduced by applying SFFSB for cathode bipolar plate and fuel cell performance is improved. Moreover, in case of using

SFFSB for the anode bipolar plate, the increase of gas diffusion force improves water removal in the anode catalyst and the membrane anode side which is responsible for the anode drying.

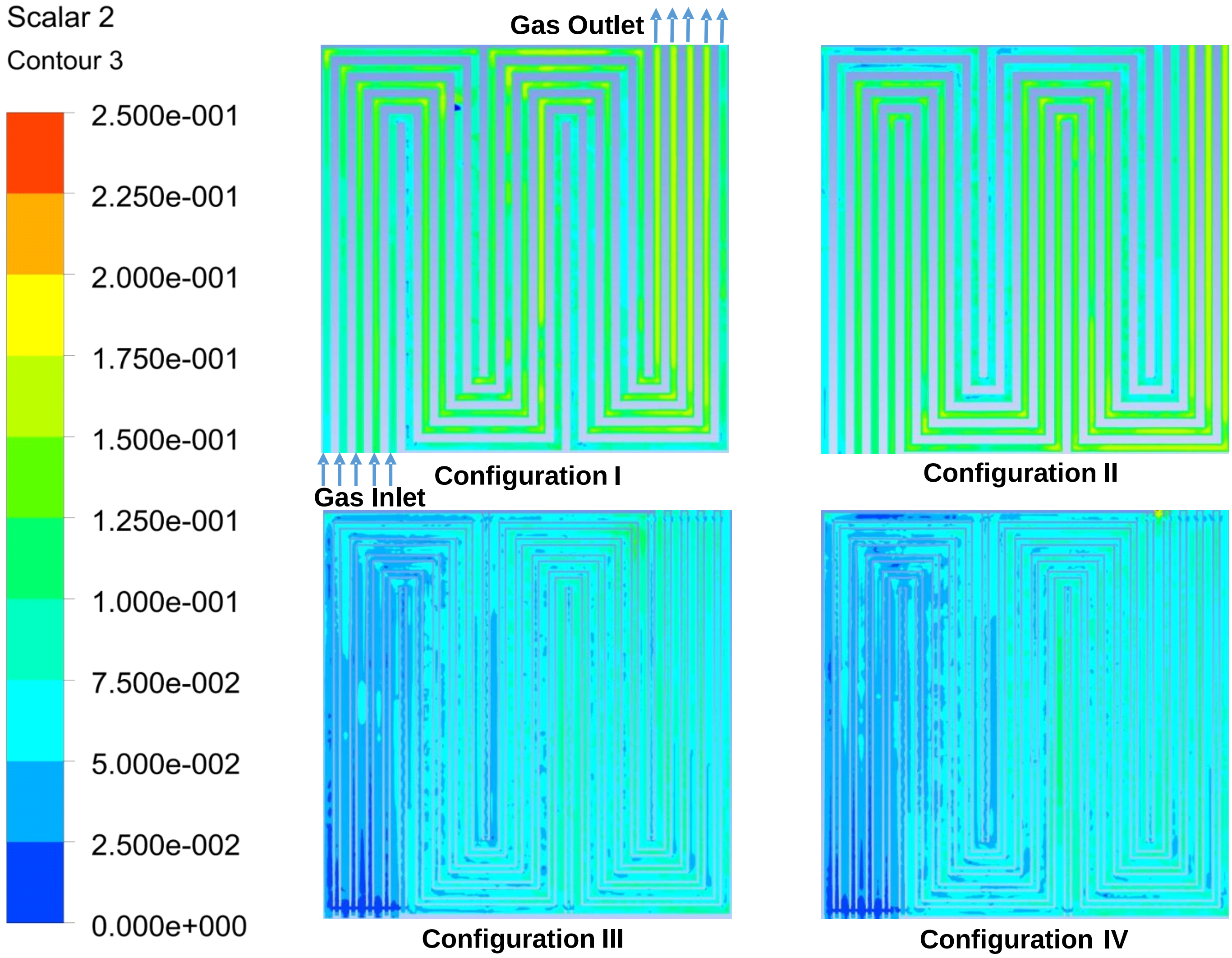

Figure 12. The comparesion of the liquid water distributions between the four flow-field configurations #I-IV at I_{avg}=1.0 A/cm^2.

3.3 Verification with the polarization and power density curves

Fig. 13 presents the current density distributions on the MEA surface of the four flow-field configurations Ⅰ-Ⅳ at I_{avg} of 1.0 A/cm^2. In the overall distributions, the local current density decreases from the inlet toward the outlet due to the lowered concentration of reacting gases. Since configurations Ⅰ-Ⅳ with different flow-field configurations have uneven electrochemical reaction, the current density distributions are changed. At the I_{ave} of 1.0 A/cm^2, the cell voltages are 0.5199 V, 0.5210 V, 0.5599 V, and 0.5588 V for the four flow-field configurations Ⅰ-Ⅳ, respectively, at I_{avg} of 1.0 A/cm^2. The differences of the cell voltages between these cases may be attributed by the differences of pressure drop, water concentrations and membrane conductivity among those which relate directly to water content and liquid water saturation of catalyst and membrane.

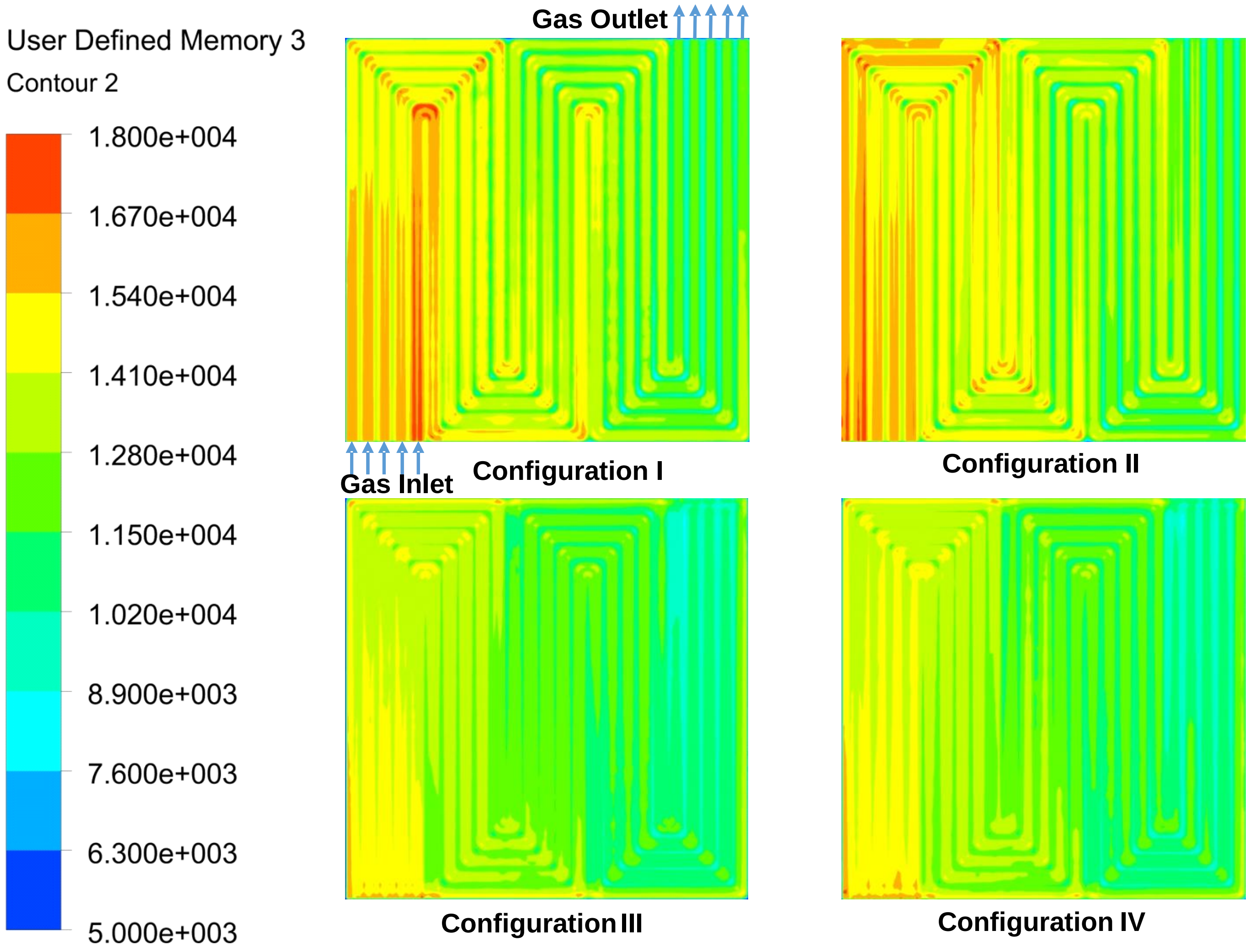

Figure 13. The comparison of current density distributions between the four flow-field configurations #I-IV at I_{avg}=1.0 A/cm^2.

To verify the maximization of power density among the performance-related parameters, the polarization and power density curves of those different flow-field configurations Ⅰ-Ⅳ are compared, and the result is given in Fig. 14. The result reveals that the power densities of configurations Ⅲ and Ⅳ are higher in comparison with the flow-field configurations Ⅰ and Ⅱ. Maximum power densities of the four flow-field configurations Ⅰ-Ⅳ are 0.5199 W/cm^2, 0.5278 W/cm^2, 0.6122 W/cm^2, and 0.6175 W/cm^2, respectively.

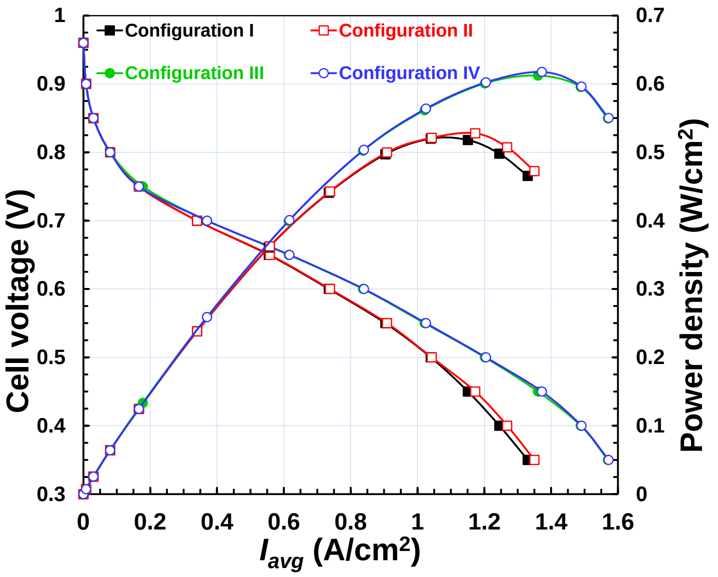

Figure 14. The comparison of the polarization and power density curves between the four flow-field configurations #I-IV.

The adoption of SFFSB at the cathode bipolar plate increases the output power density because under-rib convection enables a more effective utilization of the electrocatalysts by increasing the mass transport rates of the reactants from the flow channel to the inner catalyst layer and by significantly reducing the water flooding at the cathode.

4. CONCLUSIONS

The parametric simulations of flow-field configurations with CASFF and SFFSB in PEMFC were performed to study the distributions of pressure drop, membrane water content, and liquid water mass fractions in the electrodes, temperature, and current density over the entire surfaces, and the maximization of cell voltage at I_{avg} of 1.0 A/cm^2. Four serpentine flow-field configurations of 5-passes and 4-turns on 25 cm^2 active area were simulated numerically using the CFD software ANSYS Fluent® 14.5.

In two flow-field configurations Ⅲ and Ⅳ that SFFSB is applied at the cathode, the pressure drop is decreased because of the greater cross-sectional area for gas flow, and the decreased pressure drop results in the reduction of the load of BOP and accumulation of liquid water at the outlet. The anode liquid water mass fraction increases with increasing channel height because of increased back diffusion, while the cathode liquid water mass fraction does not depend upon the sub-channels which are ascribed mainly to the electro-osmotic drag. The increase in the anode liquid water had favorable effects of humidifying and cooling the membrane. The current and power densities in the flow-field configuration Ⅳ that CASFF and SFFSB is applied at the anode and the cathode respectively are slightly higher than those in the flow-field configuration Ⅲ that SFFSB is applied at both the anode and the cathode. The output power density is lowered due to the decreased cell voltage. In two flow-field configurations Ⅲ and Ⅳ, the under-rib convection increases the oxygen mass fraction in the under-rib regions, whereas the water from the reaction on the cathode side is physically unable to diffuse to the anode by the back diffusion and thus membrane dehydration occurs.

The findings in this work may make it possible to optimize the design of under-rib convection driven flow-field for efficient PEMFC. High cell voltage and uniform current density can be maintained by applying the favorable effects of SFFSB that minimize the pressure drop and facilitate the discharge of liquid water. Future research will focus on the numerical and experimental validations of a newly designed serpentine flow-field configuration with SFFSB in order that under-rib convection enables a more effective utilization of the electrocatalysts by increasing the mass transport rates of the reactants from the flow channel to the inner catalyst layer and by significantly reducing the water flooding at the cathode.

ACKNOWLEDGEMENTS

This work was supported by the New & Renewable Energy of the Korea Institute of Energy Technology Evaluation and Planning (KETEP) grant funded by the Korea government Ministry of Knowledge Economy (No. 2012T100100660).

References

1. H.A. Gasteiger, N. M Marković, *Science* 324, (2009) 48.
2. X. Li, I. Sabir, *Int. J. Hydrog. Energy* 30, (2005) 359.
3. M.V. Williams, H.R. Kunz, J.M. Fenton, *J. Power Sources* 135, (2004) 122.
4. J.G. Pharoah, *J. Power Sources* 144, (2005) 77.
5. J.P. Feser, A.K. Prasad, S.G. Advani, *J. Power Sources* 161, (2006) 404.
6. L. Sun, P.H. Oosthuizen, K.B. McAuley, *Int. J. Therm. Sci.* 45, (2006) 1021.
7. J. Park, M. Matsubara, X. Li, J. *Power Sources* 173, (2007) 404.
8. X.-D. Wang, Y.-Y. Duan, W.-M. Yan, D.-F. Leed, A. Sue, P.-H. Chie, *J. Power Sources* 193, (2009) 684.
9. K.-S. Choi, H.-M. Kim, S.-M. Noon, *Electrochem. Commun.* 13, (2011) 1387.
10. K.-S. Choi, B. Kim, K. Park, H.-M. Kim, *Computer & Fluids* 69, (2012) 81.
11. B. Lee, K. Park, H.-M. Kim, *Int. J. Electrochem. Sci.* 8, (2013) 219.
12. K. Park, J. Lee, H.-M. Kim, K.-S. Choi, G. Hwang, *Sci. Rep.* 4, (2014) 4592.
13. C. Xu, T.S. Zhao, *IEEE T. Energy Conver.* 29, (2014) 727.
14. C. Xu, T.S. Zhao, *Electrochem. Commun.* 9, (2007) 497.
15. X.-D. Wang, Y.-X. Huang, C.-H. Cheng, J.-Y. Jang, D.-J. Lee, W.-M. Yan, A. Suan, *Int. J. Hydrog. Energy* 35, (2010) 4247.
16. D.-H. Jeon, S. Greenway, S. Shimpalee, J.-W. Van Zee, *Int. J. Hydrog. Energy* 33, (2008) 1052.
17. K.-S. Choi, H.-M. Kim, S.-M. Noon, *Int. J. Hydrog. Energy* 36 (2011) 1613.
18. K. Park, H.-M. Kim, K.-S. Choi, *Fuel Cells* 13, (2013) 927.
19. ANSYS FLUENT Fuel Cell Modules Manual Theory Guide, Release 14.5. ANSYS, Inc., 2012.